Applied Physics Letters ARTICLE scitation.org/journal/apl

An AlGaN tunnel junction light emitting diode operating at 255 nm

Cite as: Appl. Phys. Lett. **117**, 241101 (2020); doi: 10.1063/5.0036286
Submitted: 3 November 2020 · Accepted: 27 November 2020 ·
Published Online: 14 December 2020

A. Pandey,[1] J. Gim,[2] R. Hovden,[2] and Z. Mi[1,a)]

AFFILIATIONS

[1]Department of Electrical Engineering and Computer Science, University of Michigan, 1301 Beal Avenue, Ann Arbor, Michigan 48109, USA
[2]Department of Materials Science and Engineering, University of Michigan, Ann Arbor, Michigan 48109, USA

[a)]**Author to whom correspondence should be addressed:** ztmi@umich.edu. **Tel.:** (734) 764–3963

ABSTRACT

We report on the demonstration of high-performance tunnel junction deep ultraviolet (UV) light-emitting diodes (LEDs) by using plasma-assisted molecular beam epitaxy. The device heterostructure was grown under slightly Ga-rich conditions to promote the formation of nanoscale clusters in the active region. The device operates at ∼255 nm with a maximum external quantum efficiency of 7.2% and wall-plug of 4%, which are nearly one to two orders of magnitude higher than those of previously reported tunnel junction devices operating at this wavelength. The devices exhibit highly stable emission, with a nearly constant emission peak with increasing current, due to the strong charge carrier confinement related to the presence of Ga-rich nanoclusters. Efficiency droop, however, is observed at relatively low current densities. Detailed temperature-dependent measurements suggest that the presence of efficiency droop of deep UV LEDs is largely due to electron overflow.

Light within the UV-C wavelength range (<280 nm) inactivates pathogens and can be used for the prevention of spoilage of food[1] as well as for healthcare applications.[2] Such critical applications have taken on an even more pressing need as UV-C light can effectively contain the spread of infectious diseases, making it a vital tool against the next global pandemic. Currently, mercury and xenon lamps are primarily used for these applications. AlGaN-based deep UV optoelectronic devices, however, are revolutionizing the industry, enabling much broader applications due to the absence of toxic materials, tunable emission wavelengths, significantly reduced power consumption, and relative ease of installation and use. To date, emission in the 260–280 nm range is commonly used for this purpose. Recent work has shown that emission at even shorter wavelengths (higher energies), from 255 nm to 220 nm, can be more effective at sterilization,[3] while the reduced photon penetration depth in skin can avoid the deleterious effects of human exposure to UV light.[4] At present, external quantum efficiency (EQE) over 20% has been measured for UV light-emitting diodes (LEDs) with emission at 275 nm[5] and ∼10% for LEDs at ∼265 nm.[6] For LEDs emitting at ∼255 nm, EQE in the range of 1%–3% has been commonly reported.[7–11] With proper device packaging, the highest reported EQE is only around 4.5%,[12] with very limited wall-plug efficiency (WPE) less than 4%, primarily due to the difficulty in p-type doping and the result of poor hole transport.[13,14] III-nitrides have highly asymmetric doping:[15] the hole mobilities and concentrations of AlGaN are typically over one to several orders of magnitude lower than those for electrons.[16,17] The vast imbalance in the electron and hole injection to the active region has several detrimental impacts on device performance, including significantly reduced carrier injection efficiency, severe electron overflow, and parasitic recombination outside the active region.[18–20] Recent studies further suggest that electron overflow, among other factors such as Joule heating,[21] Auger recombination[22–26] and carrier delocalization,[27,28] is a primary cause for the efficiency droop observed in UV LEDs.[20,29]

Tunnel junction structures[6,30–36] have been investigated as an alternative to resistive p-AlGaN contact layers and absorptive p-GaN contact layers[37] in UV LEDs. The reduced resistivity of the n-AlGaN contact layer helps to increase carrier injection to the active region and improve current spreading, leading to UV-C LEDs operating at 265 nm with EQE >10%.[6] Previous work has investigated the critical effect of the thickness of the tunnel junction[6,30] and doping of the p-AlGaN layers on device characteristics.[38] Earlier studies on nitride tunnel junction structures have also shown that the transport of carriers across the tunnel junction is primarily determined by trap-assisted tunneling,[39–42] indicating the crucial role of incorporating

defects around tunnel junction to maximize hole injection. To date, however, there have been no demonstrations of tunnel junction UV LEDs operating at wavelengths below 260 nm with an EQE of more than 0.1%.[32,34,36] Molecular beam epitaxy (MBE) offers distinct advantages over metal-organic chemical vapor deposition (MOCVD) for the growth of tunnel junction deep UV LEDs, due to the much more efficient incorporation of Mg-dopant incorporation in wide bandgap AlGaN.[16,43,44] Moreover, by varying the growth conditions, nanoscale clusters can be formed in Al-rich AlGaN,[45–50] which can provide strong carrier confinement and, therefore, effectively reduce nonradiative recombination as well as quantum-confined Stark effect (QCSE),[47,49,51] resulting in high efficiency deep UV emission.

In this Letter, we report on a detailed study of the epitaxy and performance characteristics of tunnel junction AlGaN deep UV LEDs operating at ∼255 nm. The device heterostructure was grown under slightly Ga-rich conditions by MBE to promote the formation of nanoscale clusters in the active region.[50,52–54] The device exhibits highly stable emission at ∼255 nm, with virtually no change in the peak emission for injection current density up to 200 A/cm^2, which is attributed to the radiative emission originating from highly localized carriers in Ga-rich regions formed in the active region. With the incorporation of an AlGaN/GaN tunnel junction, we have demonstrated 255 nm deep UV LEDs with a maximum EQE of 7.2% and WPE of 4%, which are nearly one to two orders of magnitude higher than those reported previously for tunnel junction LEDs operating at this wavelength.[32,34,35] Detailed temperature-dependent measurements further suggest several critical factors that limit the device performance, including charge carrier (hole) transport, electron overflow, and Joule heating. This work provides a promising path for achieving high efficiency far UV-C LEDs that were previously challenging.

Shown in Fig. 1(a) is the schematic of the AlGaN tunnel junction deep UV LED, which was grown using a Veeco Gen930 MBE system equipped with a radio frequency plasma-assisted nitrogen source. The device heterostructures were grown on AlN-on-sapphire templates from DOWA Holdings Co. Ltd. A nitrogen flow rate of 0.6 sccm and an RF power of 350 W were used throughout the growth, resulting in a growth rate of 160 nm/h. First, a 500-nm-thick bottom n-$Al_{0.75}Ga_{0.25}N$ contact layer was grown with a Si atom concentration of $\sim 3 \times 10^{19}$ cm^{-3}. During this growth, several steps of *in situ* annealing at elevated temperatures were performed, which can significantly improve the structural and optical properties as shown by recent studies.[55–57] The n-AlGaN was then graded up from 75% Al composition to 90% over ∼25 nm. Subsequently, the active region was grown, which consists of four AlGaN quantum wells (QWs) emitting at 255 nm, with the barrier width decreasing from 6 nm to 3.5 nm. Simulations have shown that the reduced barrier thickness closer to the p-doped side of LEDs can help improve device performance by increasing hole injection into the quantum wells, thereby leading to more even charge carrier distribution in the active region.[58,59] Following the active region, a p-doped AlGaN electron blocking layer (EBL) was grown, with Al composition graded down from 90% to 75% over 20 nm. The graded down AlGaN layer results in an enhanced p-type doping due to the strong spontaneous and piezoelectric polarization of AlGaN,[61] which can maximize the injection of holes.[60] Prior to the tunnel junction, a 25 nm highly doped p-$Al_{0.75}Ga_{0.25}N$ layer was grown, followed by a 5 nm GaN layer. The Mg atom concentration in the p-doped layers is estimated to be $\sim 5 \times 10^{19}$ cm^{-3}. Finally, a 150-nm-thick heavily doped n-$Al_{0.75}Ga_{0.25}N$ top contact layer was grown, with an annealing step included after the first 100 nm of growth. The incorporation of a thin GaN layer sandwiched between the p-AlGaN and n-AlGaN top contact layers can significantly reduce the depletion width and enhance tunneling probability by taking advantage of the large polarization charges generated at the interfaces.[61,62] The growth was carried out under slightly Ga-rich conditions, which has been previously shown to enhance dopant incorporation[16,17,48] and increase the internal quantum efficiency of AlGaN heterostructures.[47,49,50] The enhanced luminescence efficiency using this technique has been suggested to be a consequence of compositional inhomogeneities present within the AlGaN.[49] Atomic-resolution high-angle annular dark-field scanning transmission electron microscopy (HAADF-STEM) shows the ordering of Ga-rich atomic layers in the $Al_{0.75}Ga_{0.25}N$ layer; it indicates the presence of compositional non-uniformity within the layer

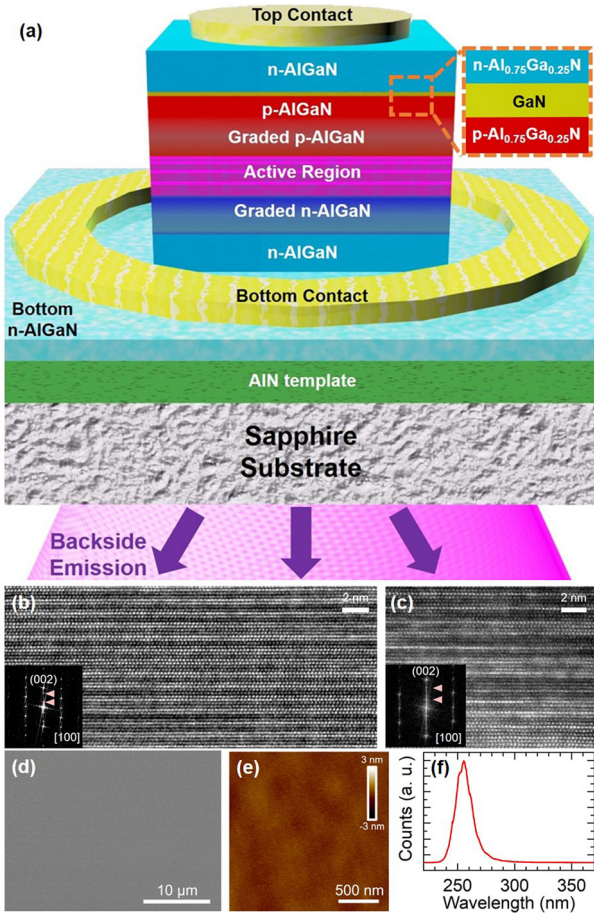

FIG. 1. (a) Schematic tunnel junction deep UV LED. The tunnel junction is shown in the marked region. (b) and (c) Atomic scale HAADF-STEM images of an $Al_{0.75}Ga_{0.25}N$ layer showing the presence of nanoscale Ga-rich layers due to compositional variation. The brighter regions correspond to the higher Ga content. FFT shows the superlattice peak (red arrows) associated with atomic ordering in wurtzite AlGaN along the c-plane direction. (d) SEM image of the sample surface after epitaxial growth showing a smooth surface over a wide area. (e) High-resolution AFM scan of the sample surface after epitaxial growth. (f) Photoluminescence spectrum of the sample measured using a 193 nm laser for excitation at room temperature.

and is consistent with previous reports[49,63] [Figs. 1(b) and 1(c)]. Low frequency background was removed to reduce contrast loss to thickness variation. Fast Fourier transform (FFT) patterns of the HAADF-STEM images exhibit ordering of the Ga-rich layer along the [001] direction; the peaks are forbidden in the electron diffraction pattern of wurtzite hexagonal symmetry. HAADF-STEM was performed using a Cs aberration-corrected JEOL 3100R05 microscope (300 keV, 22 mrad) with a detector angle from 74 to 200 mrad. While the Ga-rich growth conditions have distinct advantages, prolonged growth in this regime can lead to the formation of crystalline defects due to the presence of gallium droplets on the sample surface. To eliminate the excess Ga at the growth interface, the aforementioned annealing steps were incorporated within the growth, wherein the sample temperature was raised by 50 °C above the growth temperature, while keeping the plasma and source shutters closed. The RHEED screen was monitored to ensure that the dim, streaky RHEED pattern during growth gave way to a brighter, streaky pattern, which signifies the desorption of excess metal at the growth interface.[52,64] A scanning electron microscope (SEM) image of the sample surface after cleaning following epitaxial growth is shown in Fig. 1(d). The SEM does not show the presence of any droplets or defects on the sample surface even over large regions, showing the advantages of the annealing process. A high-resolution atomic force microscopy (AFM) scan of the surface is shown in Fig. 1(e), depicting a very smooth surface with RMS roughness below 0.5 nm. The photoluminescence of the sample measured using a 193 nm ArF excimer laser, shown in Fig. 1(f), displays an emission with a peak at 255 nm. The full width at half maximum is around 20 nm, which is a result of emission not only from the active region, but also from the graded layers surrounding the active region, as well as luminescence from the Mg-acceptor-related transitions in the p-doped layers.

The devices were fabricated using standard photolithography, etching, and contact metallization techniques. First, argon ion beam milling was used to define the device mesas, with an area of 30 μm × 30 μm. The regions surrounding the devices were etched down to the bottom n-AlGaN layer. This was followed by the deposition of a 300-nm-thick SiO_2 passivation layer. Vias were then etched into the SiO_2 to allow for the deposition of Ti/Al/Ni/Au contacts to the top and bottom n-AlGaN layers. The contacts were then annealed at 700 °C in a nitrogen ambient for 30 s. Finally, a thick reflective Al/Au contact pad was deposited over the devices to maximize light reflection toward the backside of the substrate, where a detector was placed for power measurements.

The devices were first measured in continuous-wave (CW) operation conditions using a Keithley 2400 SMU. The J-V characteristics of a representative device are shown in Fig. 2(a). The device exhibits a sharp turn-on voltage, with negligible reverse leakage current. It is noticed that the device has much improved current rectification, compared to previously reported tunnel junction devices emitting at similar wavelengths,[32] due to the reduced leakage current in the present devices. An image of a device operating at a current density of ~10 A/cm^2 is shown in the inset, demonstrating extremely bright luminescence. The electroluminescence from the device was collected using an optical fiber and analyzed through a spectrometer. The electroluminescence emission spectra measured at different injection currents are shown in Fig. 2(b). The inset is a scan over a wider range, confirming the absence of any defect-related emission at longer wavelengths that were often observed in previous studies.[34,36] The position

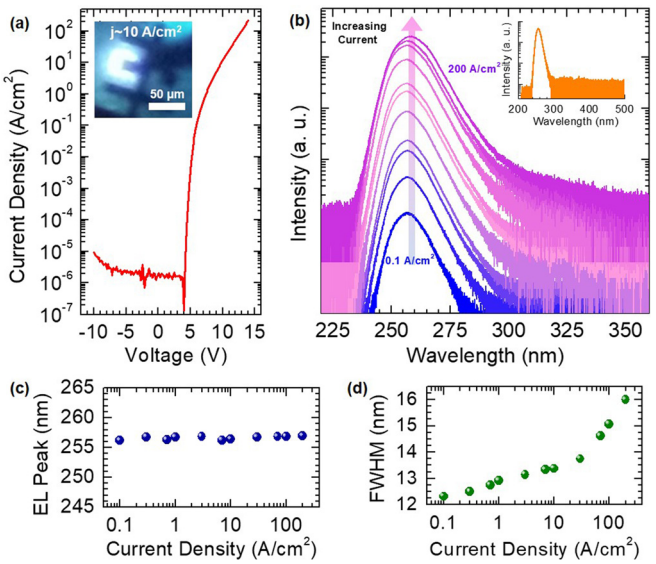

FIG. 2. (a) J–V characteristic of the tunnel junction deep UV LED. The inset shows an LED under a CW bias injection current of ~10 A/cm^2. (b) Room-temperature electroluminescence spectra measured at different injection currents. Inset: electroluminescence spectrum at an injection current of 10 A/cm^2 measured from 200 nm to 500 nm, showing the absence of defect-related emission. (c) Plot of the peak positions of the electroluminescence spectra at different injected current densities. (d) Variation of the full-width half maxima extracted from the electroluminescence spectra recorded at different injected current densities.

of the electroluminescence peak is plotted against injection current in Fig. 2(c), showing that the emission peak position is highly stable with virtually no variation for injected current densities up to 200 A/cm^2, which is in direct contrast to the expected peak variation due to the QCSE in AlGaN quantum wells. This can be explained by the strong charge carrier confinement in the Ga-rich nanoclusters in AlGaN quantum wells grown under slightly Ga-rich conditions by MBE. From Fig. 2(d), an increase in the full width at half maximum (FWHM) is seen with increasing injection current. While the increase in the FWHM is gradual up to ~10 A/cm^2, at higher current injection, the FWHM starts to rapidly increase. This broadening of the linewidth occurs primarily on the longer wavelength side of the emission peak, which can be explained by luminescence from recombination of carriers within the graded p-doped region of the device.

To determine the efficiency of the device, the emitted light from the back of the sample was collected with a Newport 818-ST2-UV photodetector with a calibrated Newport Model1919-R power meter, while the devices were probed using CW bias. As the light was only collected from the back side of the substrate, there are some losses from emission on the top and sides of the devices which were not included. Figures 3(a) and 3(b) show the variation of EQE and WPE, respectively, with injected current density. The maximum EQE and WPE measured are 5.2% and 3%, respectively. These values are nearly one to two orders of magnitude higher than those of previously reported tunnel junction devices operating at such short wavelengths.[32] The light extraction from the presented devices can be increased with proper packaging, which will further improve the efficiency.

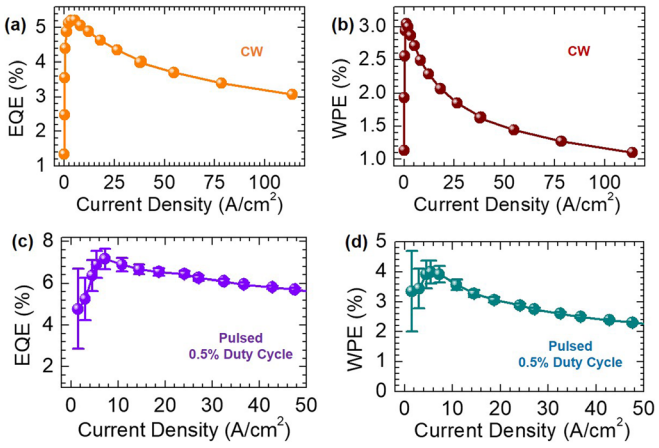

FIG. 3. (a) EQE of the tunnel junction deep UV LED vs current density measured under CW bias at room temperature. (b) WPE vs current density measured under CW bias. (c) EQE of the tunnel junction deep UV LED measured using pulsed bias with a 0.5% duty cycle. Error bars are provided. (d) WPE measured using pulsed bias with a 0.5% duty cycle. Error bars are provided.

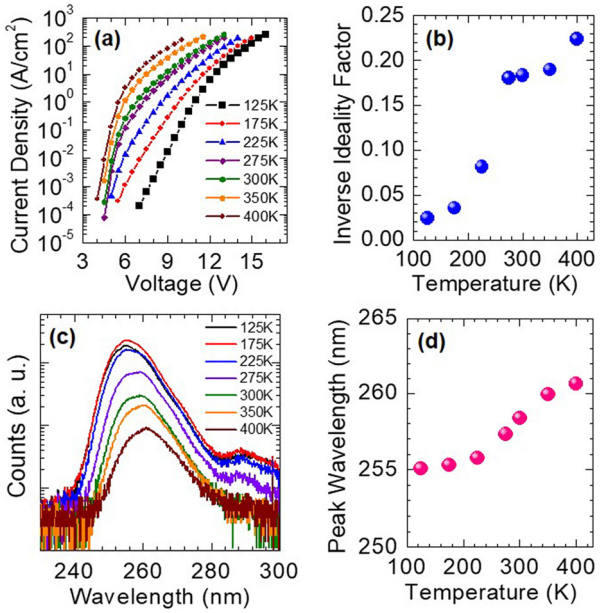

FIG. 4. (a) J–V characteristics measured at different temperatures for a tunnel junction deep UV LED. (b) Inverse of the ideality factor extracted from the J–V curves plotted against temperature. (c) Electroluminescence spectra for a device measured at different temperatures under the same injection current. (d) Variation of the peak emission wavelength with temperature.

It is also noticed that the device exhibits severe efficiency droop with further increasing current. As the samples were fabricated on sapphire substrates, heating is expected to be an issue. To mitigate the heating effect, the device efficiencies were measured under pulsed conditions, shown in Figs. 3(c) and 3(d). An AV-1010B pulse generator was used to bias the samples with a 0.5% duty cycle. A peak EQE of 7.2% and WPE of 4% were measured, respectively. Despite the improved efficiency with the reduced heating effect, the onset of efficiency droop is measured at a similar level of injection current to that under CW biasing conditions, suggesting that Joule heating may not be the primary cause for the efficiency droop. Recent studies have suggested that the primary cause for efficiency droop of deep UV LEDs is directly related to electron overflow.[18–20,65] In this study, it is observed that there is a direct correlation between the onset current density of efficiency droop with the rapid broadening of the FWHM, shown in Fig. 2(d), because of luminescence from recombination of overflowed electrons within the p-doped regions of the device. This observation is consistent with the hypothesis that the overflow of electrons from the active region is the primary cause of the efficiency droop, due to the highly asymmetric electron and hole transport of AlGaN.

The device performance, including current-voltage and electroluminescence emission, was further measured in the temperature range of 100–400 K under CW biasing conditions. Shown in Fig. 4(a) are the current–voltage characteristics measured at different temperatures. The measured current at similar bias shows a significant increase with temperature. The device remains operational even at low temperatures, despite the high Mg acceptor ionization energy, which can be explained by the involvement of tunneling transport of holes in the depletion region.[16,43,66,67] Recent studies suggest that the characteristic tunneling energy for hole transport is directly related to the Mg acceptor activation energy of Al(Ga)N and can be significantly reduced with enhanced Mg dopant incorporation, due to the Mg acceptor level dispersion at very high doping concentrations.[17,43] At room temperature, the ideality factor is derived to be ∼5.8, which is comparable to other III-nitride LEDs,[67–69] in spite of the large bandgap and the presence of a tunnel junction. The inverse of the ideality factor is plotted against temperature in Fig. 4(b). A continuous decrease in the ideality factor is measured for the device as temperature is increased, which can be explained by the growing dominance of diffusion current in the depletion region with increasing temperature, due to the more efficient hole current injection. The electroluminescence spectra were also measured at different temperatures at a similar current density around 50 A/cm^2, shown in Fig. 4(c). The peak position is plotted in Fig. 4(d), and an expected blue shift is observed with decreasing temperature. The S-shaped temperature dependence of the curve is consistent with the presence of significant alloy disorder and nanoclusters[70,71] as a result of the Ga-rich nanoclusters present in the active region [Fig. 1(b)]. A small peak at ∼290 nm is also observed. This can be explained by the increased internal quantum efficiency at low temperatures of the luminescence from overflowed carriers recombining within the p-doped region. At higher temperatures, this peak is too weak to detect. This observation confirms that the UV LEDs have severe electron overflow. Moreover, a sharp decrease in electroluminescence intensity was observed in the range of 225 K–400 K, which illustrates the significance of carrier delocalization and thermal effects in inhibiting efficient radiative recombination. The decrease in electroluminescence at temperatures above room temperature exemplifies the importance in conducting heat away from the active region when devices are operated at high current densities for high-power applications.

In conclusion, we have demonstrated high performance tunnel junction deep UV LEDs by using plasma-assisted MBE. The device operates at ∼255 nm with a maximum EQE of 7.2% and WPE of 4%, which are nearly one to two orders of magnitude higher than those of previously reported tunnel junction devices operating at this

wavelength.[32,34] The devices exhibit highly stable emission, with a nearly constant emission peak with increasing current, due to the strong charge carrier confinement related to the presence of Ga-rich nanoclusters. However, the device suffered from efficiency droop at relatively low current densities. Detailed temperature-dependent measurements suggest that the presence of severe efficiency droop of deep UV LEDs is largely due to electron overflow. Furthermore, temperature-dependent measurements have shown the impact of thermal effects on the electrical and emission properties of the device. The device performance can be further improved with proper packaging and thermal management.

This work was supported by the Blue Sky research program in the College of Engineering at the University of Michigan and the National Science Foundation (Grant No. DMR-1807984). The authors would like to thank Professor Elaheh Ahmadi from the Electrical Engineering and Computer Science department at the University of Michigan for the use of her cryostat used in the temperature-dependent measurements. Some intellectual property related to this work was licensed to NS Nanotech Inc., which was co-founded by Z. Mi.

DATA AVAILABILITY

The data that support the findings of this study are available from the corresponding author upon reasonable request.

REFERENCES

[1]V. M. Gomez-Lopez, P. Ragaert, J. Debevere, and F. Devlieghere, Trends Food Sci. Technol. **18**(9), 464–473 (2007).
[2]T. Dai, M. S. Vrahas, C. K. Murray, and M. R. Hamblin, Expert Rev. Anti-Infect. Ther. **10**(2), 185–195 (2012).
[3]M. Buonanno, D. Welch, I. Shuryak, and D. J. Brenner, Sci. Rep. **10**(1), 10285 (2020).
[4]M. Raeiszadeh and B. Adeli, ACS Photonics **7**(11), 2941–2951 (2020).
[5]T. Takano, T. Mino, J. Sakai, N. Noguchi, K. Tsubaki, and H. Hirayama, Appl. Phys. Express **10**(3), 031002 (2017).
[6]A. Pandey, W. J. Shin, J. Gim, R. Hovden, and Z. Mi, Photonics Res. **8**(3), 331–337 (2020).
[7]V. Adivarahan, W. H. Sun, A. Chitnis, M. Shatalov, S. Wu, H. Maruska, and M. A. Khan, Appl. Phys. Lett. **85**(12), 2175–2177 (2004).
[8]C. Pernot, S. Fukahori, T. Inazu, T. Fujita, M. Kim, Y. Nagasawa, A. Hirano, M. Ippommatsu, M. Iwaya, and S. Kamiyama, Phys. Status Solidi A **208**(7), 1594–1596 (2011).
[9]A. Fujioka, K. Asada, H. Yamada, T. Ohtsuka, T. Ogawa, T. Kosugi, D. Kishikawa, and T. Mukai, Semicond. Sci. Technol. **29**(8), 084005 (2014).
[10]C. Pernot, M. Kim, S. Fukahori, T. Inazu, T. Fujita, Y. Nagasawa, A. Hirano, M. Ippommatsu, M. Iwaya, and S. Kamiyama, Appl. Phys. Express **3**(6), 061004 (2010).
[11]H. Hirayama, T. Yatabe, N. Noguchi, T. Ohashi, and N. Kamata, Appl. Phys. Lett. **91**(7), 071901 (2007).
[12]M. Ichikawa, A. Fujioka, T. Kosugi, S. Endo, H. Sagawa, H. Tamaki, T. Mukai, M. Uomoto, and T. Shimatsu, Appl. Phys. Express **9**(7), 072101 (2016).
[13]C. Stampfl and C. Van de Walle, Phys. Rev. B **65**(15), 155212 (2002).
[14]M. Nakarmi, N. Nepal, C. Ugolini, T. Altahtamouni, J. Lin, and H. Jiang, Appl. Phys. Lett. **89**(15), 152120 (2006).
[15]J. L. Lyons, A. Janotti, and C. G. Van de Walle, Phys. Rev. Lett. **108**(15), 156403 (2012).
[16]A. Pandey, X. Liu, Z. Deng, W. Shin, D. Laleyan, K. Mashooq, E. Reid, E. Kioupakis, P. Bhattacharya, and Z. Mi, Phys. Rev. Mater. **3**(5), 053401 (2019).
[17]Y.-H. Liang and E. Towe, Appl. Phys. Rev. **5**(1), 011107 (2018).
[18]G.-B. Lin, D. Meyaard, J. Cho, E. F. Schubert, H. Shim, and C. Sone, Appl. Phys. Lett. **100**(16), 161106 (2012).
[19]D. S. Meyaard, G.-B. Lin, Q. Shan, J. Cho, E. F. Schubert, H. Shim, M.-H. Kim, and C. Sone, Appl. Phys. Lett. **99**(25), 251115 (2011).
[20]X. Hai, R. Rashid, S. Sadaf, Z. Mi, and S. Zhao, Appl. Phys. Lett. **114**(10), 101104 (2019).
[21]W. Sun, M. Shatalov, J. Deng, X. Hu, J. Yang, A. Lunev, Y. Bilenko, M. Shur, and R. Gaska, Appl. Phys. Lett. **96**(6), 061102 (2010).
[22]J. Piprek, Phys. Status Solidi A **207**(10), 2217–2225 (2010).
[23]J. Cho, E. F. Schubert, and J. K. Kim, Laser Photonics Rev. **7**(3), 408–421 (2013).
[24]J. Iveland, L. Martinelli, J. Peretti, J. S. Speck, and C. Weisbuch, Phys. Rev. Lett. **110**(17), 177406 (2013).
[25]F. Nippert, M. Tollabi Mazraehno, M. J. Davies, M. P. Hoffmann, H.-J. Lugauer, T. Kure, M. Kneissl, A. Hoffmann, and M. R. Wagner, Appl. Phys. Lett. **113**(7), 071107 (2018).
[26]C. Frankerl, F. Nippert, A. Gomez-Iglesias, M. P. Hoffmann, C. Brandl, H.-J. Lugauer, R. Zeisel, A. Hoffmann, and M. J. Davies, Appl. Phys. Lett. **117**(10), 102107 (2020).
[27]J. Mickevičius, G. Tamulaitis, M. Shur, M. Shatalov, J. Yang, and R. Gaska, Appl. Phys. Lett. **101**(21), 211902 (2012).
[28]J. Mickevičius, G. Tamulaitis, M. Shur, M. Shatalov, J. Yang, and R. Gaska, Appl. Phys. Lett. **103**(1), 011906 (2013).
[29]J. Yun, J.-I. Shim, and H. Hirayama, Appl. Phys. Express **8**(2), 022104 (2015).
[30]C. Kuhn, L. Sulmoni, M. Guttmann, J. Glaab, N. Susilo, T. Wernicke, M. Weyers, and M. Kneissl, Photonics Res. **7**(5), B7–B11 (2019).
[31]Y. Zhang, Z. Jamal-Eddine, F. Akyol, S. Bajaj, J. M. Johnson, G. Calderon, A. A. Allerman, M. W. Moseley, A. M. Armstrong, and J. Hwang, Appl. Phys. Lett. **112**(7), 071107 (2018).
[32]Y. Zhang, S. Krishnamoorthy, F. Akyol, S. Bajaj, A. A. Allerman, M. W. Moseley, A. M. Armstrong, and S. Rajan, Appl. Phys. Lett. **110**(20), 201102 (2017).
[33]Y. Zhang, S. Krishnamoorthy, F. Akyol, J. M. Johnson, A. A. Allerman, M. W. Moseley, A. M. Armstrong, J. Hwang, and S. Rajan, Appl. Phys. Lett. **111**(5), 051104 (2017).
[34]S. Zhao, S. Sadaf, S. Vanka, Y. Wang, R. Rashid, and Z. Mi, Appl. Phys. Lett. **109**(20), 201106 (2016).
[35]S. Sadaf, S. Zhao, Y. Wu, Y.-H. Ra, X. Liu, S. Vanka, and Z. Mi, Nano Lett. **17**(2), 1212–1218 (2017).
[36]S. Bharadwaj, K. Lee, S. Islam, V. Protasenko, H. G. Xing, and D. Jena, "Tunnel-junction p-contact sub-250 nm deep-UV LEDs," in 2017 Conference on Lasers and Electro-Optics (CLEO), San Jose, CA, 2017, pp. 1–2.
[37]H. Hirayama, N. Maeda, S. Fujikawa, S. Toyoda, and N. Kamata, Jpn. J. Appl. Phys., Part 1 **53**(10), 100209 (2014).
[38]Y. Zhang, S. Krishnamoorthy, F. Akyol, A. A. Allerman, M. W. Moseley, A. M. Armstrong, and S. Rajan, Appl. Phys. Lett. **109**(19), 191105 (2016).
[39]M. Auf der Maur, B. Galler, I. Pietzonka, M. Strassburg, H. Lugauer, and A. Di Carlo, Appl. Phys. Lett. **105**(13), 133504 (2014).
[40]L. Sang, M. Liao, N. Ikeda, Y. Koide, and M. Sumiya, Appl. Phys. Lett. **99**(16), 161109 (2011).
[41]E. C. Young, B. P. Yonkee, F. Wu, S. H. Oh, S. P. DenBaars, S. Nakamura, and J. S. Speck, Appl. Phys. Express **9**(2), 022102 (2016).
[42]E. Vadiee, E. A. Clinton, H. McFavilen, A. S. Weidenbach, Z. Engel, C. Matthews, C. Zhang, C. Arena, R. R. King, and C. B. Honsberg, Appl. Phys. Express **11**(8), 082304 (2018).
[43]Y. Wu, D. A. Laleyan, Z. Deng, C. Ahn, A. F. Aiello, A. Pandey, X. Liu, P. Wang, K. Sun, and E. Ahmadi, Adv. Electron. Mater. **6**(9), 2000337 (2020).
[44]N. H. Tran, B. H. Le, S. Zhao, and Z. Mi, Appl. Phys. Lett. **110**(3), 032102 (2017).
[45]S. Zhao, S. Woo, M. Bugnet, X. Liu, J. Kang, G. Botton, and Z. Mi, Nano Lett. **15**(12), 7801–7807 (2015).
[46]S. Zhao, S. Woo, S. Sadaf, Y. Wu, A. Pofelski, D. Laleyan, R. Rashid, Y. Wang, G. Botton, and Z. Mi, APL Mater. **4**(8), 086115 (2016).
[47]Y. Liao, C. Thomidis, C.-K. Kao, and T. D. Moustakas, Appl. Phys. Lett. **98**(8), 081110 (2011).
[48]T. D. Moustakas and A. Bhattacharyya, Phys. Status Solidi C **9**(3–4), 580–583 (2012).
[49]A. Bhattacharyya, T. Moustakas, L. Zhou, D. J. Smith, and W. Hug, Appl. Phys. Lett. **94**(18), 181907 (2009).

[50]T. D. Moustakas, MRS Commun. **6**(3), 247–269 (2016).
[51]V. N. Jmerik, D. V. Nechaev, S. Rouvimov, V. V. Ratnikov, P. S. Kop'ev, M. V. Rzheutski, E. V. Lutsenko, G. P. Yablonskii, M. Aljohenii, and A. Aljerwii, J. Mater. Res. **30**(19), 2871 (2015).
[52]V. Jmerik, E. Lutsenko, and S. Ivanov, Phys. Status Solidi A **210**(3), 439–450 (2013).
[53]V. Y. Davydov, V. Jmerik, E. Roginskii, Y. E. Kitaev, Y. Beltukov, M. Smirnov, D. Nechaev, A. Smirnov, I. Eliseyev, and P. Brunkov, Semiconductors **53**(11), 1479–1488 (2019).
[54]E. Iliopoulos, K. Ludwig, Jr., and T. Moustakas, J. Phys. Chem. Solids **64**(9–10), 1525–1532 (2003).
[55]D. A. Laleyan, N. Fernández-Delgado, E. T. Reid, P. Wang, A. Pandey, G. A. Botton, and Z. Mi, Appl. Phys. Lett. **116**(15), 152102 (2020).
[56]N. Susilo, S. Hagedorn, D. Jaeger, H. Miyake, U. Zeimer, C. Reich, B. Neuschulz, L. Sulmoni, M. Guttmann, and F. Mehnke, Appl. Phys. Lett. **112**(4), 041110 (2018).
[57]H. Miyake, C.-H. Lin, K. Tokoro, and K. Hiramatsu, J. Cryst. Growth **456**, 155–159 (2016).
[58]S. J. Kim and T. G. Kim, Phys. Status Solidi A **211**(3), 656–660 (2014).
[59]M.-C. Tsai, S.-H. Yen, Y.-C. Lu, and Y.-K. Kuo, IEEE Photonics Technol. Lett. **23**(2), 76–78 (2011).
[60]J. Simon, V. Protasenko, C. Lian, H. Xing, and D. Jena, Science **327**(5961), 60–64 (2010).
[61]Y. Zhang, S. Krishnamoorthy, J. M. Johnson, F. Akyol, A. Allerman, M. W. Moseley, A. Armstrong, J. Hwang, and S. Rajan, Appl. Phys. Lett. **106**(14), 141103 (2015).
[62]D. Jena, J. Simon, A. Wang, Y. Cao, K. Goodman, J. Verma, S. Ganguly, G. Li, K. Karda, and V. Protasenko, Phys. Status Solidi A **208**(7), 1511–1516 (2011).
[63]A. Aiello, A. Pandey, A. Bhattacharya, J. Gim, X. Liu, D. A. Laleyan, R. Hovden, Z. Mi, and P. Bhattacharya, J. Cryst. Growth **508**, 66–71 (2019).
[64]H. Okumura, K. Balakrishnan, H. Hamaguchi, T. Koizumi, S. Chichibu, H. Nakanishi, T. Nagatomo, and S. Yoshida, J. Cryst. Growth **189**, 364–369 (1998).
[65]H.-H. Chen, J. S. Speck, C. Weisbuch, and Y.-R. Wu, Appl. Phys. Lett. **113**(15), 153504 (2018).
[66]X. Liu, A. Pandey, D. A. Laleyan, K. Mashooq, E. T. Reid, W. J. Shin, and Z. Mi, Semicond. Sci. Technol. **33**(8), 085005 (2018).
[67]K. Lee, P. Parbrook, T. Wang, J. Bai, F. Ranalli, R. Airey, and G. Hill, Phys. Status Solidi B **247**(7), 1761–1763 (2010).
[68]K. Mayes, A. Yasan, R. McClintock, D. Shiell, S. Darvish, P. Kung, and M. Razeghi, Appl. Phys. Lett. **84**(7), 1046–1048 (2004).
[69]K. Lee, P. Parbrook, T. Wang, J. Bai, F. Ranalli, R. Airey, and G. Hill, J. Cryst. Growth **311**(10), 2857–2859 (2009).
[70]P. G. Eliseev, P. Perlin, J. Lee, and M. Osiński, Appl. Phys. Lett. **71**(5), 569–571 (1997).
[71]A. Bell, S. Srinivasan, C. Plumlee, H. Omiya, F. Ponce, J. Christen, S. Tanaka, A. Fujioka, and Y. Nakagawa, J. Appl. Phys. **95**(9), 4670–4674 (2004).